SANDIA REPORT
SAND2005-6273
Unlimited Release
Printed October 2005

A Turbulence Model for Buoyant Flows Based on Vorticity Generation

Vernon F. Nicolette, Sheldon R. Tieszen, Amalia R. Black,
Stefan P. Domino, and Timothy J. O'Hern

Prepared by
Sandia National Laboratories
Albuquerque, New Mexico 87185 and Livermore, California 94550

Sandia is a multiprogram laboratory operated by Sandia Corporation,
a Lockheed Martin Company, for the United States Department of Energy's
National Nuclear Security Administration under Contract DE-AC04-94AL85000.

Issued by Sandia National Laboratories, operated for the United States Department of Energy by Sandia Corporation.

Available to DOE and DOE contractors from
U.S. Department of Energy
Office of Scientific and Technical Information
P.O. Box 62
Oak Ridge, TN 37831

Telephone: (865) 576-8401
Facsimile: (865) 576-5728
E-Mail: reports@adonis.osti.gov
Online ordering: http://www.osti.gov/bridge

Available to the public from
U.S. Department of Commerce
National Technical Information Service
5285 Port Royal Rd
Springfield, VA 22161

Telephone: (800) 553-6847
Facsimile: (703) 605-6900
E-Mail: orders@ntis.fedworld.gov
Online order: http://www.ntis.gov/help/ordermethods.asp?loc=7-4-0#online

SAND2005-6273
Unlimited Release
Printed October 2005

A Turbulence Model for Buoyant Flows Based on Vorticity Generation

Vernon F. Nicolette and Sheldon R. Tieszen
Fire Science and Technology Department

Amalia R. Black
V&UQ Process Department

Stefan P. Domino
Engineering Sciences Department

Timothy J. O'Hern
Thermal/Fluid Experimental Sciences Department

Sandia National Laboratories
P.O. Box 5800
Albuquerque, New Mexico 87185-1135

Abstract

A turbulence model for buoyant flows has been developed in the context of a k-ε turbulence modeling approach. A production term is added to the turbulent kinetic energy equation based on dimensional reasoning using an appropriate time scale for buoyancy-induced turbulence taken from the vorticity conservation equation. The resulting turbulence model is calibrated against far field helium-air spread rate data, and validated with near source, strongly buoyant helium plume data sets. This model is more numerically stable and gives better predictions over a much broader range of mesh densities than the standard k-ε model for these strongly buoyant flows.

Acknowledgments

This work has been sponsored by various organizations within Sandia National Laboratories, including Surety (Org. 12300), ESRF Tech Base (9100), and M&PM (9100). Helpful comments were provided by A.L. Brown (SNL), G.H. Evans (SNL), W.L. Oberkampf (SNL), P.E. Desjardin (SUNY Buffalo), and W.P. Jones (Imperial College, UK). The experimental work and associated data processing were conducted with the assistance of Amarante Martinez, Mark Nissen, and Andy Gerhart of Sandia National Laboratories. The authors are grateful to William Mell (U. of Utah) for sharing his experimental helium data with us.

CONTENTS

FIGURES

TABLE

NOMENCLATURE

Alphabetical

BVG	buoyant vorticity generation
CFD	computational fluid dynamics
CVFEM	control volume finite element model
C_μ	constant in eddy diffusivity expression
$C_{\varepsilon 1}$, $C_{\varepsilon 2}$, $C_{\varepsilon 3}$	constants in ε-equation
D	plume inlet diameter
FLAME	test facility name at Sandia National Laboratories
g	gravitational acceleration
G_B	buoyancy generated production of k
GGDH	generalized gradient diffusion hypothesis
k	turbulent kinetic energy
K	thousand
L	length scale; stream-wise distance from inlet
LHS	left-hand side
M	million
MUSCL	Monotonic Upwind Scheme for Conservation Laws
NIST	National Institute of Standards and Technology
p	pressure
P_k	shear generated production of k
PIV	particle image velocimetry
RANS	Reynolds Averaged Navier-Stokes
Re	Reynolds number, $V_O D/\nu$
RHS	right-hand side
Ri	Richardson number, $(\rho_e - \rho_p)gD/(\rho_e V_0^2)$
Sc_ε	Schmidt number for ε-equation
Sc_k	Schmidt number for k-equation
S_{ij}	rate of strain tensor
SNL	Sandia National Laboratories
t	time
u	velocity
URANS	unsteady Reynolds averaged Navier-Stokes
V_0	plume inlet velocity
w	out of plane velocity
x	spatial coordinate; distance downstream from origin

Greek

δ_{ij}	Kronecker delta function
Δ	arithmetic difference
ε	dissipation of turbulent kinetic energy
μ	dynamic viscosity
ν	kinematic viscosity

ν_t	turbulent (kinematic) eddy viscosity
ρ	density
τ	time scale
ω	vorticity
$\vec{\nabla}$	gradient

Superscripts

-	Reynolds average
~	Favre average
"	fluctuation about the Favre mean value

Subscripts

B	buoyant
e	ambient
i,j	tensor indices
l	laminar
p	plume
s	shear
t	turbulent

1 INTRODUCTION

1.1 Purpose

Numerical simulation of buoyancy-driven flows is of interest for many engineering applications. Computational fluid dynamics (CFD) tools appropriate for buoyancy-driven flow modeling are under development or being utilized by many researchers (e.g., Cox [1], Worthy et al. [2]). Since large-scale buoyant flow fields are always turbulent, these tools have a representation of turbulence embedded in them (i.e., some model of turbulence). The purpose of this work is to describe the development of a buoyant turbulence model that is applicable to buoyancy-driven flows as well as in more traditional momentum-dominated applications, and demonstrate the application of such a model for several data sets in the literature.

1.2 Motivation

The motivation for this work stems from problems encountered in simulating buoyant plumes and pool fires with standard turbulence models. For such flows, the resulting turbulence is due primarily to buoyancy (and not shear) effects. Standard models for turbulence (such as the k-ε model) have been developed based upon shear-generated turbulence mechanisms, and not based upon buoyancy-generated turbulence mechanisms. Hence these models encounter problems when applied to flows that are primarily buoyancy-driven. While the focus of this work is on non-reacting flows, there is nothing inherent in the modeling that precludes its use for reacting flows as well.

1.3 Historical Perspective

The turbulence models most commonly employed in commercial CFD tools (or production codes, i.e., codes that are *not* research codes) are based upon the k-ε model of turbulence (Launder and Spalding [3], Jones and Launder [4]). Such models have well-known strengths and weaknesses, and are used primarily because they are robust, i.e., they yield reasonable results for many different scenarios of interest. The use of the k-ε turbulence model for buoyant flow simulation is somewhat surprising, as the model was derived for flows with primarily *shear-generated* turbulence. Some CFD simulation tools employ a standard k-ε turbulence model (some with low Reynolds number modifications) along with a correction term to account for thermal stratification effects that tend to dampen turbulence in the hot gas layer near the ceiling of an enclosure (see for example, Cox [1]). This correction was first suggested by Rodi [5], and is referred to herein as “Rodi’s model.”

A number of turbulence models have been proposed for buoyant flows, and it is not the purpose of this work to extensively review these studies. Of particular note, however, is the work of Daly and Harlow [6] who developed the Generalized Gradient Diffusion Hypothesis (or GGDH). This model is noteworthy because it has served as a basis for the development of several other representations of buoyancy-generated turbulence for non-reacting and reacting flows (see for example, Ince and Launder [7], Worthy et al. [2]). Recently, some investigators have attempted

to include the effects of buoyancy-generated turbulence in CFD fire simulations (beyond the use of Rodi's model) based on the work of Ince and Launder [7]. Some of these investigations have been limited to fires on (or between) flat surfaces (walls), since such problems lend themselves to a parabolic formulation of the transport equations (Wang and Joulain [8], Wang, Joulain, and Most [9]).

Another promising model has been proposed by Chomiak and Nisbet [10]. Their model assumes that both scalar transport and turbulence generation arising from pressure-density interactions in flames are attributable to the motion of large-scale turbulent thermals superimposed on the shear turbulence mechanism. The velocity of the large-scale thermals is directly related to the mean pressure gradient and local density differences in the flame.

1.4 Present Work

While the above models have shown promise, the authors believe they are lacking in that they do not adequately model the physics leading to the generation of buoyant turbulence. For example, Chomiak and Nisbet [10] relied upon similarities to flows involving bubble dynamics in developing key parts of their formulation. The starting assumption for the current study is that buoyancy results in turbulent kinetic energy production through gravitational (hydrostatic) and baroclinic (hydrodynamic) vorticity generation (c.f., Tieszen, et al. [11]). Through vorticity transport, the resultant vorticity forms vortical structures that collide, tangle, and comprise the turbulent flow. From this starting assumption, the present work develops a model of buoyancy-induced turbulence based on an appropriate time scale for buoyancy-induced vorticity generation taken from the vorticity conservation equation, and infers a characteristic length scale for the resultant turbulence. The authors feel that this is a more physically meaningful starting point for model development than the assumptions used in previous work.

2 MODEL DEVELOPMENT

The standard equations relevant to momentum transport and turbulence are presented first to establish a background. A derivation of the buoyancy-generated turbulence modifications follows. Note that while the standard k-ε model is used below, a similar derivation could be performed for other turbulence modeling frameworks (e.g., k-ω).

2.1 Conservation of Momentum

The momentum equation (in tensor notation) can be written as

$$\frac{\partial}{\partial t}\overline{\rho}\widetilde{u}_i + \frac{\partial}{\partial x_j}\left(\overline{\rho}\widetilde{u}_i\widetilde{u}_j\right) = -\frac{\partial \overline{p}}{\partial x_i} + \overline{\rho g_i} + \frac{\partial}{\partial x_j}\left(\mu_l\left(\frac{\partial \widetilde{u}_i}{\partial x_j} + \frac{\partial \widetilde{u}_j}{\partial x_i}\right) - \overline{\rho u_i'' u_j''}\right) \tag{1}$$

where variables with an overbar are Reynolds averaged, variables with a tilde are Favre averaged (density weighted), and the double prime indicates a fluctuation relative to the Favre average. The last term on the right-hand side (RHS) involving the velocity fluctuations is commonly referred to as the Reynolds stress term. It requires modeling in order to close the set of equations (which also includes conservation of mass, species, and energy (or enthalpy)).

Invoking the Boussinesq eddy viscosity assumption, the Reynolds stress term can be written as

$$-\overline{\rho u_i'' u_j''} = \mu_t\left(\frac{\partial \widetilde{u}_i}{\partial x_j} + \frac{\partial \widetilde{u}_j}{\partial x_i}\right) - \tfrac{2}{3}\delta_{ij}\overline{\rho}k \tag{2}$$

where μ_t is the turbulent eddy viscosity, defined as

$$\mu_t = c_\mu \rho\left(k^2/\varepsilon\right). \tag{3}$$

When expressions for k and ε are put forth, the Reynolds stress term can be evaluated, a closed set of equations is obtained, and a solution to the suite of momentum, mass, species, and enthalpy equations can (in theory) be reached.

2.2 Equations for k and ε

The standard form of the k-ε equations for buoyant flow is as follows. The equation for turbulent kinetic energy can be written as

$$\frac{\partial}{\partial t}\rho k + \frac{\partial}{\partial x_i}\left(\overline{\rho}\widetilde{u}_i k\right) = \frac{\partial}{\partial x_i}\left(\overline{\rho}\left(\frac{\nu_t}{Sc_k}\right)\frac{\partial k}{\partial x_i}\right) + P_k - \overline{\rho}\varepsilon + G_B. \tag{4}$$

The term G_B represents a source term due to buoyancy, and needs to be modeled (the term P_k is the standard source term due to shear). The equation for the dissipation of turbulent kinetic energy can be written as

$$\frac{\partial}{\partial t}\overline{\rho}\varepsilon + \frac{\partial}{\partial x_i}\left(\overline{\rho}\widetilde{u}_i\varepsilon\right) = \frac{\partial}{\partial x_i}\left(\overline{\rho}\left(\frac{\nu_t}{Sc_\varepsilon}\right)\frac{\partial \varepsilon}{\partial x_i}\right) + C_{\varepsilon 1}\frac{\varepsilon}{k}P_k - C_{\varepsilon 2}\overline{\rho}\frac{\varepsilon^2}{k} + C_{\varepsilon 3}\frac{\varepsilon}{k}G_B \tag{5}$$

where, for generality, a term containing G_B has also been introduced, similar to Eq. (4). The term G_B arises from an unclosed term in the turbulent kinetic energy equation expressed as (c.f., Chomiak and Nisbet [10], Borghi and Escudie [12])

$$G_B = \overline{-u_i'' \frac{\partial p}{\partial x_i}}. \tag{6}$$

2.4 A New Model for Buoyancy-Generated Turbulence

The closure model for Eq. (6) is derived based on consistency, dimensional reasoning, and phenomenological arguments. The shear-generated turbulence production term, P_k, is expressed as

$$P_k = 2\mu_t S_{ij}\frac{\partial \widetilde{u}_i}{\partial x_j}, \tag{7}$$

where S_{ij} is the rate of strain tensor (units of inverse time). $\frac{\partial \widetilde{u}_i}{\partial x_j}$ also has units of inverse time, so that shear production has a form

$$P_k \sim \mu_t \Big/ \tau_s^{\,2}, \tag{8}$$

where the characteristic time scale for the production of turbulence is proportional to the mean shear gradients. From Eq. (4),

$$\frac{\partial}{\partial t}\overline{\rho}k = P_k + G_B. \tag{9}$$

Consistency suggests a similar closure be employed for the buoyant production term, yielding

$$P_k + G_B \sim \mu_t\left(1\Big/\tau_S^{\,2} + 1\Big/\tau_B^{\,2}\right). \tag{10}$$

An appropriate time scale for buoyancy-generated turbulence can be taken from the vorticity transport equation. For variable density flows, a vorticity generation term arises. The subsequent transport of the buoyantly-generated vorticity results in turbulence. It is assumed that the generation of vorticity is the rate-limiting step in the production of buoyant turbulence, and thus defines the appropriate characteristic time scale. From the vorticity equation, we note that a production time scale is

$$1/\tau_B{}^2 \sim \frac{1}{\rho^2}\left\|\vec{\nabla}\rho\times\vec{\nabla}p\right\|, \tag{11}$$

where the double vertical bars indicate that a magnitude must be taken (since the resultant of the cross product is itself a vector). This time scale is based on the mechanism for buoyant vorticity generation (BVG), and is inversely proportional to the square root of the cross product of the local density gradient and the pressure gradient. Note that the pressure in Eq. (11) consists of both a hydrostatic and a dynamic component. Therefore there are two components that make a contribution to the generation of buoyant turbulence: a hydrostatic (or gravitational) component and a hydrodynamic (or baroclinic) component.

Substituting the buoyant time scale, τ_B, from Eq. (11) into Eq. (10) yields

$$G_B \sim \mu_t \frac{\left\|\vec{\nabla}\rho\times\vec{\nabla}p\right\|}{\rho^2}, \tag{12}$$

where we have dropped the overbar on density for convenience (Reynolds averaging implicitly assumed). Similarly, we will drop the tilde over k and ε in what follows (Favre averaging implicitly assumed). Adding in a constant of proportionality, C_{BVG}, and using the definition of kinematic viscosity, the source term to the k-equation due to buoyancy-generated turbulence becomes

$$G_B = C_{BVG}\nu_t \frac{\left\|\vec{\nabla}\rho\times\vec{\nabla}p\right\|}{\rho}. \tag{13}$$

Note that C_{BVG} is not the only constant that needs to be determined for the model. The equation for the dissipation of turbulent kinetic energy, Eq. (5), also contains a constant ($C_{\varepsilon 3}$) that must be determined.

In flows that are initially laminar, Eq. (13) predicts that the buoyant production will be zero. This is not the correct limiting behavior. In laminar flows the correct diffusion coefficient is the laminar coefficient. Thus, to enable the model in initially laminar flows, the laminar viscosity is added to the turbulent viscosity resulting in

$$G_B = C_{BVG}(\nu_t + \nu)\frac{\left\|\vec{\nabla}\rho \times \vec{\nabla}p\right\|}{\rho}. \tag{14}$$

Note that without density gradients in the flow, G_B will be zero everywhere and the model will simplify to the standard k-ε model. It is hoped that the derivation is sufficiently clear that users of treatments other than k-ε can derive buoyant production in the context of their own models.

Using dimensional reasoning, scalings can be derived. Comparing Eq. (13) to Eq. (6), we can write

$$u_i'' \sim \nu_t \left\| \left(\frac{\vec{\nabla}\rho}{\rho} \right) \right\|. \tag{15}$$

Thus the characteristic turbulent velocity fluctuation that arises from buoyant generation is proportional to the turbulent diffusivity and the scaled density gradient. Clearly from Eq. (13), the appropriate correlation between pressure and density is the cross product of the density gradient and the pressure gradient. If the density gradient and the pressure gradient are perfectly aligned (or 180° out of phase), then the cross product is zero, and there is no correlation between them that will produce turbulent kinetic energy (on average). This corresponds to stable and neutrally stable conditions. If some misalignment of the density gradient and the pressure gradient exists, then a correlation between them exists, as given by the cross product, and the result is the production of turbulent kinetic energy.

Noting that it is also possible to express the turbulent viscosity in terms of a length scale, L, as

$$\nu_t \sim k^{1/2} L \sim u'' L, \tag{16}$$

it is then possible to define the appropriate length scale for buoyancy-generated turbulence from Eqs. (15)-(16):

$$L_B \sim \frac{\nu_t}{u''} \sim \left(\rho \Big/ \frac{\partial \rho}{\partial x} \right). \tag{17}$$

This simply states that the appropriate length scale for buoyancy-generated turbulence is the physical distance over which a density gradient exists.

2.5 Implementation Issues

If the present model is implemented into a code using an essentially incompressible scheme, as many production-level CFD codes do, problems have been observed with the model during the first several time steps. In order to conserve mass with the incompressible assumption, large pressure gradients can be generated during the first few time steps near the inlet and outlet

boundaries. Although these large gradients in pressure generally only last for the first several time steps, it can complicate the solution by generating significant values of G_B in regions far removed from the plume itself. One way around this problem is to implement a limiter on the density gradient. A recommendation is to use something such as

$$\vec{\nabla}\rho = 0 \quad \text{if} \quad \frac{\Delta\rho}{\rho} < 10^{-6} \tag{18}$$

where $\Delta\rho$ is the same density difference used in the evaluation of $\vec{\nabla}\rho$. Another possibility is to use only shear-generated source terms for the first few time steps/iterations, and then switch on the BVG contribution.

For fluid cells adjacent to a solid boundary, the usual log-law wall functions are used. No modification was made herein for fluid cells in the log-law region. The contribution of the buoyant production and dissipation was assumed to be negligible in this region, although it could be added in if desired. The authors do not believe this addition would change the results significantly. Unlike shear-dominated flows in which turbulence production in the boundary layer near a surface usually dominates the turbulence field, in buoyancy-generated flows the turbulence production occurs at any location in the fluid where misaligned density and pressure gradients exist. Consequently, the production of buoyant turbulence in the fluid cells in the log-law region is not crucial to the simulation of the turbulence field, since the production mechanism exists for quite a distance from the surface (as determined by the distance over which a significant density gradient exists).

It is essential to evaluate the gradients given in Eq. (14) consistently for both boundary and domain fluid cells. It is especially important that the gradients in fluid cells adjacent to injection cells are properly evaluated; otherwise a situation can result in which it is impossible to stabilize the flow. As expected, the model has been found to be sensitive to implementation issues such as the consistency of gradient evaluations at boundaries, the stencil used for calculation of k, and whether or not a low Reynolds number modification is used in the standard k-ε model.

3 MODEL IMPLEMENTATION, VERIFICATION, AND CALIBRATION

The BVG model (Eq. (14)) was implemented into the SIERRA/Fuego fire simulation tool (described below) for verification and calibration.

3.1 Fuego Description

SIERRA/Fuego (or simply, Fuego) is a low-Mach-number, turbulent reacting flow code (Domino, et al. [13]). In variable density flows we use the Favre-averaged form of the unsteady transport equations describing the transport of heat, mass, and momentum. Closure of the turbulent stresses is obtained through an eddy viscosity assumption. The two-equation k-ε turbulence model is used to determine the eddy viscosity. The governing turbulent transport equations are written in integral form and discretized on unstructured meshes using a control volume finite element method (CVFEM).

Primitive variables are located at the vertices of the finite elements. The finite volumes are centered about the nodes and assembled on an element-by-element basis. The integration points are determined by the surfaces connected between the element centroid, the element face centroids, and the edge centroids. Therefore, integration points, over which surface fluxes are evaluated, are located at sub-face centers. Linear shape functions are used for the interpolation of properties and the computation of gradients within the element.

A segregated, approximate projection scheme is the numerical solution method. Since the primitive variables are colocated, a modified momentum interpolation method is employed to avoid pressure-velocity decoupling. This method adds a pressure stabilizing term proportional to the fourth order spatial derivative of pressure. A backward Euler time integration approach that includes the effect of variable density is used. The current method is first order accurate in time. Picard looping (iteration within each time step) ensures time accuracy of the solution. Steady solutions are obtained using a pseudo-transient time stepping algorithm.

Several upwind schemes are supported for the evaluation of convective fluxes at integration points. Each upwind method is blended with a centered scheme as the cell Peclet number falls below two. In general, assembling element by element, in lieu of neighbor contributions, limits the order of the convection coefficient. The supported standard “lower order methods” include first order upwind and a skew upwind approach that requires element face intersections. A Monotonic Upwind Scheme for Conservation Laws (MUSCL, cf. Hirsh [14]) with van Leer limiter is also available.

3.2 Implementation and Verification of BVG Model in Fuego

The BVG model is verified to be implemented correctly within Fuego (see Domino [15] for a detailed description; only a brief overview is given here). The verification approach was a modified unit test of the BVG model. Specifically, an actual Fuego simulation was performed

and point wise values of the subcontrol volume weighted turbulence production term were checked against hand calculations.

The simulation input file was used to prescribe constant initial values of turbulent kinetic energy, turbulence dissipation rate, and linear profiles of temperature and pressure for flow in a vertical duct. Based on the linear profiles of both pressure and temperature (through which density is calculated using the ideal gas law) and given the initial conditions for turbulence quantities (through which eddy viscosity is calculated), the subcontrol volume assembled value of the turbulence production rate due to buoyant vorticity generation was given at all locations within the domain.

This unit test procedure ensures a non-invasive methodology to check the values of the calculated BVG production term against an analytic model. Moreover, given that any solid mesh rotation will result in a constant value of production term (assuming the initial conditions for temperature and pressure are properly rotated respectively with the mesh), the model implementation has been verified even for mesh rotations. Refinement studies were carried out to demonstrate that the numerical implementation is convergent to the analytic model. Further details concerning verification of the BVG model in Fuego can be found in Domino [15].

3.3 Far Field Spread Rate Calibration Against NIST Plume

Whereas some authors use different constants when applying the k-ε model to round jets/plumes, we have chosen to adopt the standard constant set (c.f., Launder and Spalding [3]). While the standard constant set applies best to planar jets, and different constant sets are sometimes applied to round jets, it was deemed best to adopt the standard set of constants in the work that follows, as this approach is the most widely used in the literature.

The BVG model requires calibration of two constants (see Eqs. (5) and (14)). The constant in Eq. (5), $C_{\varepsilon 3}$, was determined to be zero via parametric comparisons between numerical simulations and the data for far field spread rate of buoyant plumes and jets. The constant in Eq. (14) was calibrated against the same data. Based on velocity half-widths, Fischer et al. [16] gives the far field spreading rate for buoyant jets as 0.107 ± 0.003, and the far field spreading rate for buoyant plumes as 0.100 ± 0.005.

A buoyant helium plume experiment (referred to below as the NIST plume) conducted by Johnson at the National Institute of Standards and Technology (NIST) Building and Fire Research Laboratory (see Mell [17]) was simulated. This plume had non-zero initial momentum, as it had an entrance velocity of 0.487 m/s (Ri = 2.6 and Re = 291 based upon the nozzle diameter of 0.073 m). Therefore the spread rate would be expected to be somewhere in between the spreading rates for the buoyant plume and buoyant jet given above. A coarse mesh (65K nodes), a medium mesh (198K nodes), and a fine mesh (515K nodes) were used to simulate the NIST plume with several values for the BVG constant of Eq. (14). All simulations were 3D and unsteady, and were carried out until a steady solution had been obtained. Results were relatively insensitive to the initial turbulence levels at the inlet (not available in the experimental data), and were examined at a downstream location of x/D= 105 diameters. Note that the fully developed

region is generally regarded as beginning prior to 100 diameters downstream. Table 1 shows the spreading rate (based on velocity half-width) of the plume versus downstream distance as a function of the BVG constant (Eq. (14)) and mesh density. A constant of 0.35 is seen to provide a reasonable fit to the buoyant plume and jet data cited above for the coarse, medium, and fine mesh simulations.

Table 1. Calculated plume far field spreading rate (x/D=105) versus BVG constant and mesh density. Experimental data ranges from 0.100 to 0.107.

BVG Constant	Mesh	Spreading Rate
0.25	coarse	0.093
0.30	coarse	0.097
0.35	coarse	0.104
0.35	medium	0.105
0.35	fine	0.105
0.40	fine	0.130

4 MODEL/DATA COMPARISONS

Predictions are compared with data for several plumes near their source. These data represent a very difficult challenge to turbulence models. At a plume source, the density differences are the strongest, the velocity gradients are low, and the turbulence is suppressed to the extent possible in both the plume and free stream. Thus, the buoyant production of turbulence is maximized, the shear production of turbulence is minimized, and the inlet conditions are laminar. The strong buoyant production of turbulence results in a rapid laminar to turbulent transition, within a few centimeters of the source based on photographic evidence obtained from the experimental data presented in Sections 4.2 and 4.3 below. In each case, the centerline vertical velocity as a function of elevation from the source is taken as the measure of agreement, although other quantities and spatial locations are also examined.

4.1 NIST Plume Centerline Velocity Comparison

Centerline vertical velocity data from the helium plume experiment (Mell [17]) used previously for the calibration of the constant in the BVG model is shown in Figure 1 along with the numerical results for the coarse, medium, and fine meshes. Since the BVG constant was calibrated based on far field spread rate, the comparison of centerline velocities represents a somewhat independent check of the model. Reasonably good agreement (within 8%) is shown in the figure for the medium, and fine meshes, with a peak numerical centerline velocity of 2.25 m/s versus 2.45 m/s in the experiment. The results indicate that the model predicts a slightly faster rise to the peak centerline velocity, which also decays sooner than in the experimental results. The coarse mesh results indicate that the coarse mesh is too under-resolved to capture the peak centerline velocity, but that the far field velocity and slope approach that of the two finer meshes.

4.2 SNL Helium Plume Test 18 Comparison

To obtain additional data for comparison to turbulence models such as those developed here, several helium plume experiments were performed as described in detail in O'Hern et al. [18]. A brief description of the experimental setup is given here for Test 18, which differs in boundary conditions from those reported in [18]. Experiments were performed in FLAME, a 6.1-m (20-ft) cubical enclosure with an annular air supply surrounding the plume source and an exhaust through a central chimney. The plume source is 1 meter in diameter with a spatially uniform (± 6%) helium mixture velocity of 0.13 m/s. Air was supplied at 0.077 m/s. The Reynolds number was Re = 1220, where D is the diameter of the plume source (1 meter), V_0 is the inlet velocity, and ν is the kinematic viscosity. The Richardson number was Ri = 520, where ρ_e is the external (air) density, ρ_p is the plume density, and g is gravitational acceleration. The large Richardson number is indicative of a strongly buoyant plume with low initial momentum. Such flows typically present a difficult challenge for shear-based turbulence models.

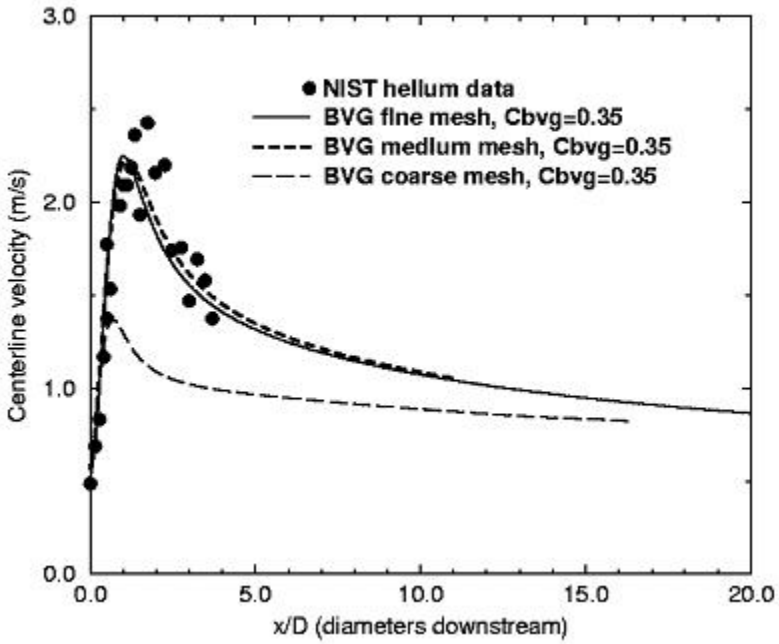

Figure 1. Near field center line velocity comparison for NIST helium plume (data from Mell [17]). Coarse mesh = 65K nodes. Medium mesh = 198K nodes. Fine mesh = 515K nodes.

The test procedure was to start the flow of the helium mixture (molecular weight = 5.4 g/mol helium with acetone vapor and oxygen; for fluorescence measurements not presented here, see O'Hern et al. [18]), and allow a couple of minutes of flow to establish stable conditions. Data collection occurred for about 8 seconds. Inlet, outlet, and boundary measurements were made to characterize mass, momentum, and energy boundary conditions.

Particle image velocimetry (PIV) measured velocity in the helium plume and surrounding air. High-speed 35-mm motion picture cameras acquired images and two-frame iterative cross-correlation PIV analysis was performed using PIV Sleuth software (Christensen, Soloff, and Adrian [19]). The final interrogation region was approximately .021 m square, with a 50% overlap between regions. PIV analysis was conducted on approximately 1000 frames of film from the helium plume, covering 6 puff cycles of the flow. The turbulent kinetic energy is derived from the fluctuating velocity fields as the sum of the normal stresses in the three directions. Since the current study involved only inplane PIV, the out-of-plane normal stress is not known; however, it is not expected to be zero. With the assumption that the strength of streamwise and tangential vorticity are the same, a common assumption made in determining the turbulent kinetic energy from two-dimensional data is that the out-of-plane fluctuations $\overline{w''^2}$ are equal to the cross-stream fluctuations $\overline{u''^2}$.

In addition to the velocity boundary conditions specified above, a turbulence intensity of 0.1% was assumed for the helium injection, since video footage indicated an essentially laminar inflow of helium. Numerical results were insensitive to turbulence intensities of the air inflow, as the air

injection occurs almost a meter below the pedestal where helium is injected. All simulations performed for this case were unsteady, 3D simulations. Steady results were obtained for the 2 meshes used in the simulation (250K and 500K nodes).

Figure 2 shows the centerline velocities for both the experiment and the simulations. Peak values experimentally are 2.15 m/s, while the model prediction is ~2.5 m/s for both meshes. However, the plume was slightly off-center in the experiment (roughly 0.10–0.15 m), so the experimental data is also shown at a radial offset of 0.10 m (peak value of 2.56 m/s). Both the numerical results are in good agreement with the measured peak velocity (using the radially offset value). The numerical results for both meshes indicate a somewhat faster rise to peak velocity, as well as a quicker decrease in centerline velocity, than the data. It is interesting to note that the 250K grid results follow the radially offset data more closely than the 500K mesh results. The reason for this is addressed in the Discussion section.

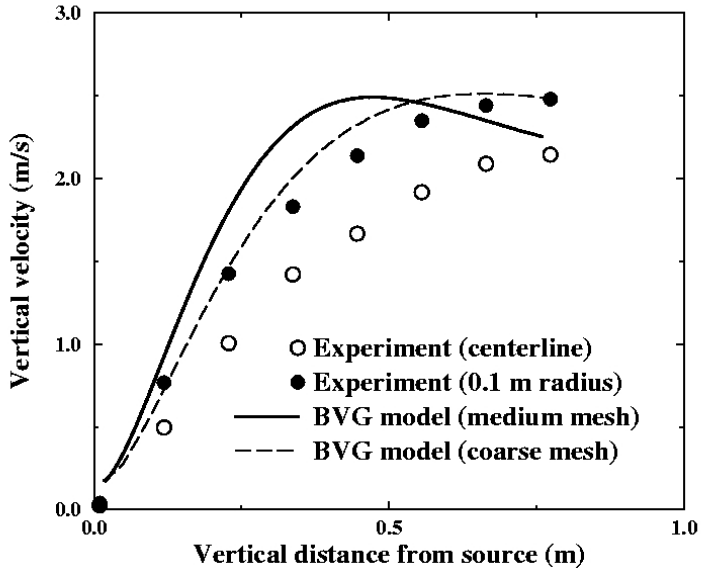

Figure 2. Centerline velocity comparison for SNL helium plume Test 18. Plume is slightly shifted in the experiment, lying ~0.1 m off-center. Coarse (250K) and medium (500K) mesh results shown.

The radial offset in the plume can be clearly seen in the experimental results of Figure 3, which shows the experimental vertical velocity contours in a 2D vertical plane through the plume center, as well as the numerical simulation results using the BVG model for the 500K mesh. Peak values of vertical velocity (2.56 m/s experimental vs. 2.49 m/s numerical) and the qualitative shape of the velocity contours are well predicted. The breadth of the plume (as denoted by the velocity contours) indicates that the numerical results are somewhat more viscous than the experimental results in this near field region of the flow.

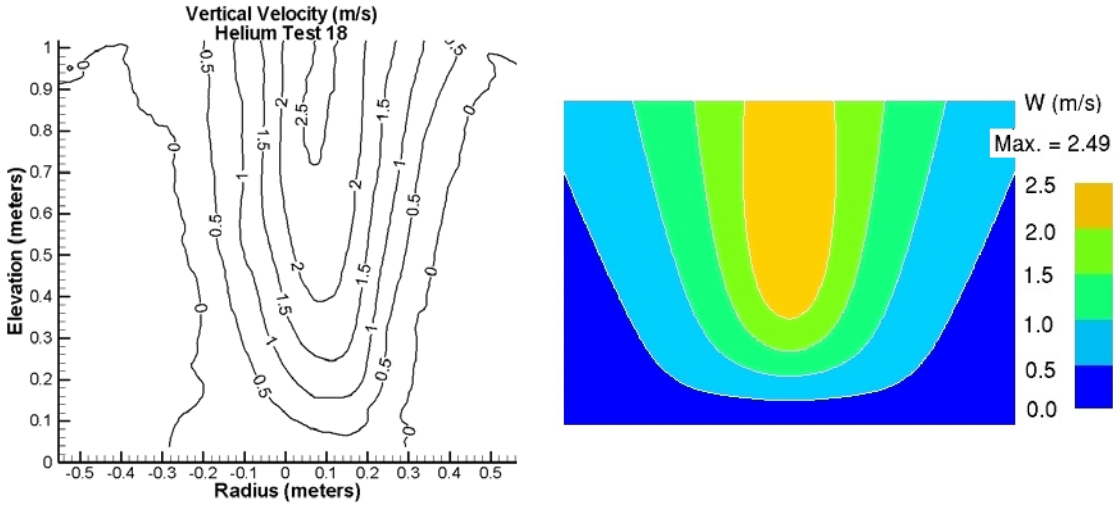

Figure 3. Vertical velocity contours for SNL helium plume Test 18. LHS: Experimental. RHS: BVG model results for a similar cut plane (500K mesh), and with the same axis scaling as the data. Note that the experimental data is shifted about 0.1 m to the right of the centerline.

Figure 4 shows the experimentally inferred distribution of turbulent kinetic energy within the flow field, subject to the assumptions discussed above, as well as the numerical simulation results using the BVG model for the 500K mesh. The numerical peak value (0.614 m^2/s^2) is 22% larger than the peak experimental value (0.508 m^2/s^2). Once again, the breadth of the plume indicates that the numerical results are somewhat more viscous than the experimental results, as evidenced by sharper gradients in the experimental profiles near the edge of the plume.

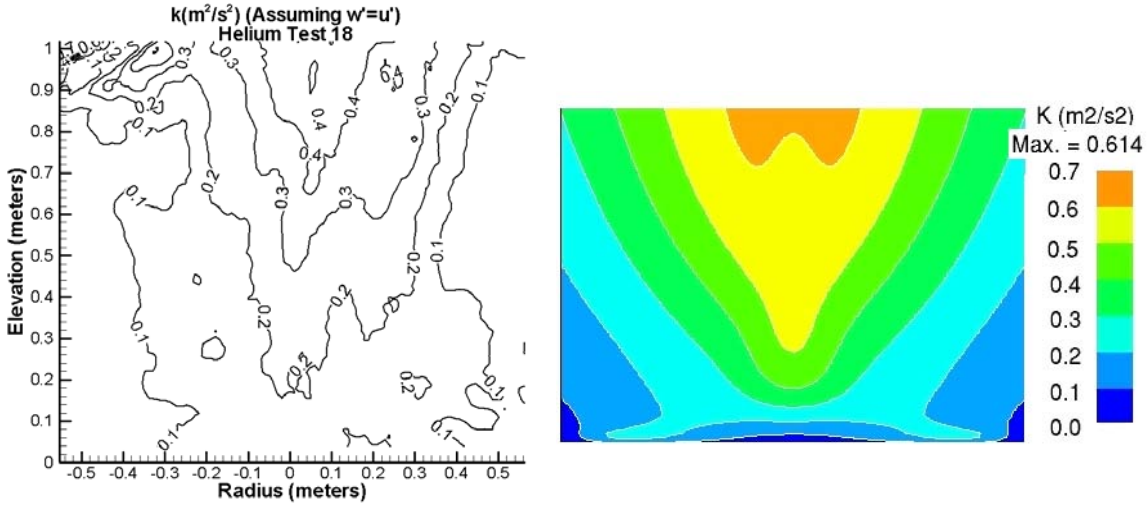

Figure 4. Turbulent kinetic energy contours for SNL helium plume Test 18. LHS: Experiment. RHS: BVG model results for a similar cut plane (500K mesh), and with the same axis scaling as the data.

4.3 SNL Helium Plume Tests #25, 29, 32, 36 Comparison

As an additional test of the model, data from four repeat tests (Tests #25, #29, #32 and #36, referred to below as the SNL test ensemble) at an inlet plume velocity approximately three times that of Test 18 were averaged and used as input conditions for the numerical calculations. The helium mixture (molecular weight = 5.4 g/mol) plume velocity was specified to be 0.34 m/s with a turbulence intensity of 0.1% based on experimental images that suggest that the flow entering the domain is laminar. Within two standard deviations, the Reynolds number is 3200 +/- 0.6% and the Richardson number is 76 +/- 6.5%. The larger Reynolds number and smaller Richardson number relative to the previous comparison data set (Test 18) imply that the ensemble data set will have a higher initial momentum relative to the buoyancy of the plume. The implications of this are discussed in the Discussion section.

The inlet air velocity was specified to be 0.148 m/s with a turbulence intensity of 6% based on the temporal variation in the data. For the numerical simulations, a constant total pressure condition of 81.7 kPa was specified at the exit of the chimney (corresponding to the atmospheric pressure at the FLAME facility test site). Along the surface of the FLAME facility, no-slip, isothermal walls were specified.

Simulations were conducted with four different grid densities (250K, 500K, 1M, and 2M nodes) to determine the sensitivity of the solution to grid size. Mesh refinement was accomplished by doubling the grid points in the vicinity of the helium plume and adding grid points away from the plume to smoothly vary the clustering of points. Figure 5 shows a cross section of the 500K node mesh along the centerline of the FLAME facility. The grid lines are clustered toward the helium inlet in all three directions. In addition, Figure 5 shows density contours from the BVG simulation and a standard k-ε simulation for the region where experimental data was obtained. The results obtained with the BVG model are steady for the 500K mesh, while those obtained with the standard k-ε model are unsteady for any given time plane.

Figures 6 and 7 show simulation and experimental results for the vertical velocity and turbulent kinetic energy profiles for the 500K node solution. In general, the shapes of the profiles are qualitatively similar, and peak magnitudes for both the velocity and the turbulent kinetic energy are somewhat over-predicted. The peak velocity was 4.3 m/s for the 500K node solution and 3.1 m/s for the experimental data. The peak turbulent kinetic energy was 1.2 m^2/s^2 for the 500K node solution and 1.0 m^2/s^2 for the experimental data.

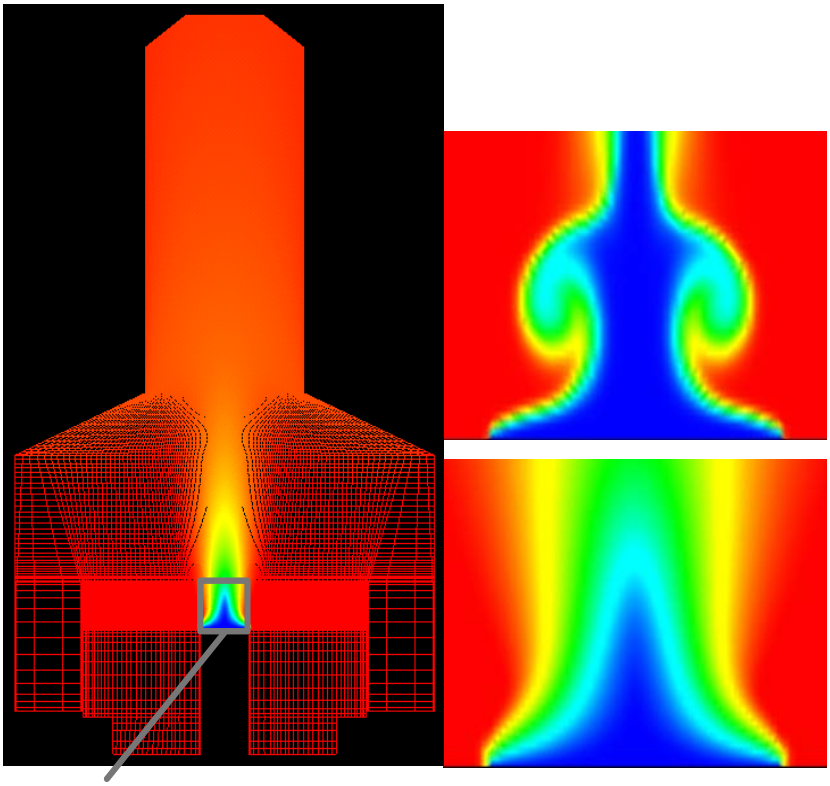

Figure 5. Flame facility computational mesh cross section (500K) for SNL helium test ensemble with BVG model density contours overlaid (LHS). Standard k-ε model produces unsteady results, as evidenced by the density contours shown in upper RHS of figure. BVG model produces steady results for 250K and 500K grids, as evidenced by the density contours shown in lower RHS of figure.

Figure 8 shows the results of the mesh refinement study on the centerline vertical velocity profile with elevation. The 250K node mesh is under-resolved and predicts a somewhat lower centerline velocity profile than the data. The 500K node mesh shows a more rapid rise to peak velocity than the data, consistent with the results for the NIST plume and the lower-velocity helium test. Recall that the constant is set on the far field spread rate, so it can be presumed that if there were data at higher elevations, the differences between the simulation and data would continue to decrease. The BVG model simulations produced steady solutions using the 250K and 500K node grids; however, the 1M and 2M node grids resulted in unsteady solutions. The reasons for the unsteady solutions, and possible interpretations of them, are discussed below. The results shown in Figure 8 are the result of density-weighting and time-averaging (i.e., Favre averaging) of the unsteady results. The unsteady results were time-averaged over a 10-second interval (6-7 puffs), similar to the interval used to time average the experimental data.

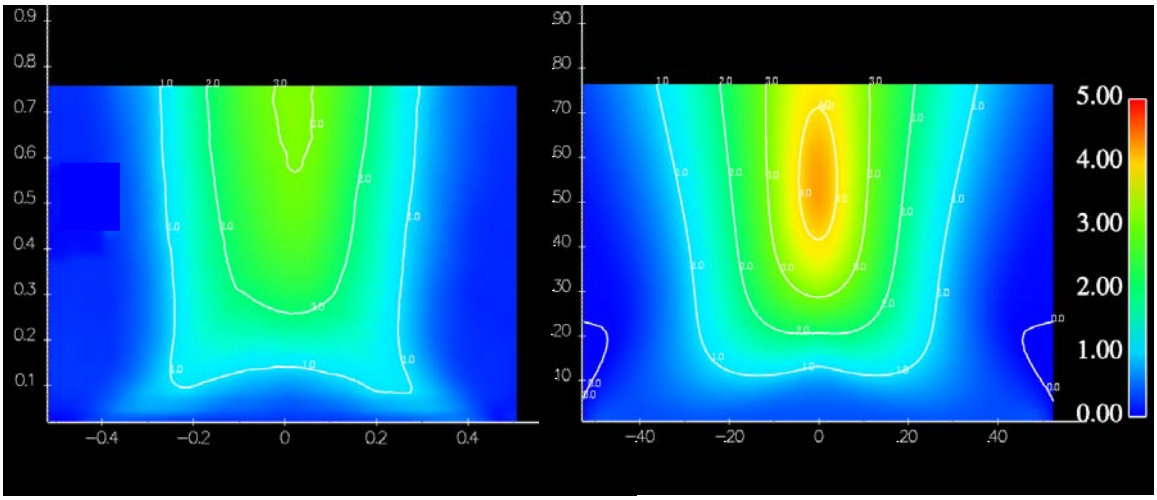

Figure 6. Vertical velocity contours for SNL helium test ensemble. LHS: Experimental (Peak = 3.1m/s). RHS: BVG model, 500K mesh, steady solution (Peak = 4.3 m/s).

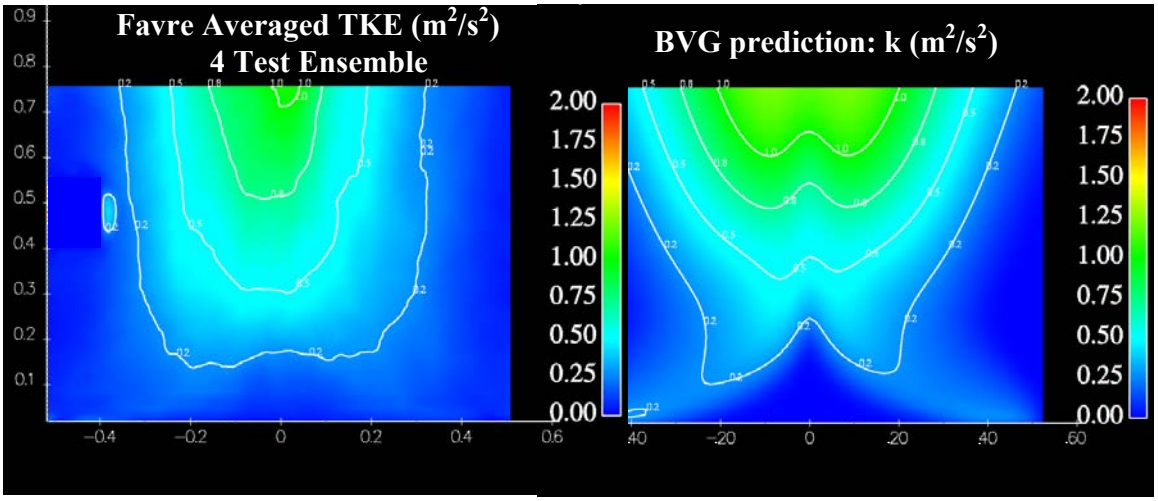

Figure 7. Turbulent kinetic energy contours for SNL helium test ensemble. LHS: Experimental (Peak = 1.0 m^2/s^2). RHS: BVG model, 500K node mesh, steady solution (Peak = 1.2 m^2/s^2).

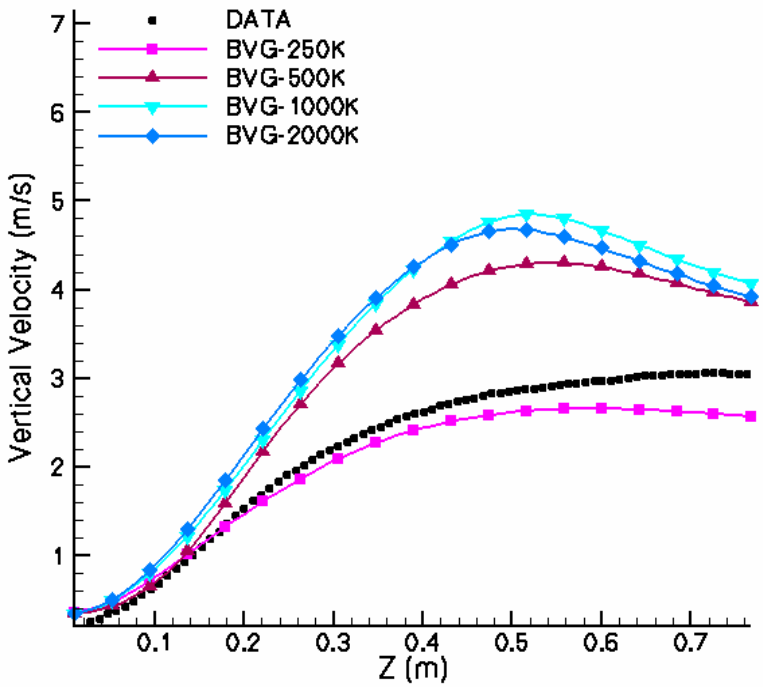

Figure 8. Vertical velocity profiles for BVG model simulations of SNL helium test ensemble. Note that the 250K and 500K mesh solutions are steady, while the other solutions are puffing.

5 DISCUSSION

Several subtleties/complexities exist regarding the comparisons of simulations and experiments that warrant further discussion.

5.1 Laminar to Turbulence Transition

In order to maximize the effects of buoyancy and its effect on turbulence production, the data sets used for validation in this study have minimized the inlet momentum and have laminar inlet conditions. The flows undergo a laminar-to-turbulent transition just above the source. The effect of the transition to turbulence on time-averaged centerline velocities is to lower the peak velocity relative to what a laminar flow would produce due to turbulent spreading of the momentum. Thus, a predicted centerline velocity in excess of the data (or a faster rise in centerline velocity versus elevation) relative to the data is an indication that the turbulence model is not capturing the transition.

In all the comparisons, the BVG model predicts a faster rise to peak velocity than the data. This observation suggests that the BVG model is not transitioning as fast as the data indicates. The delay is most evident in Figure 8 (ensemble test), for which the model also results in an over-prediction of the centerline peak vertical velocity for the higher mesh densities. The delay in transition (and hence a more rapid rise to the peak centerline velocity) is also seen in the results of Figure 1 (Test 18). However, the lower initial momentum of the plume in Test 18 results in earlier core collapse. This collapse allows for faster (with respect to elevation) radial penetration of buoyancy- and shear-generated turbulence produced along the helium/air interface to the plume centerline. The authors speculate that this faster radial penetration results in better agreement of peak centerline velocities for the lower inlet velocity test (Test 18) relative to the higher inlet velocity ensemble test.

Accurate prediction of laminar to turbulence transition with eddy viscosity closure models is notoriously unreliable. The use of the laminar viscosity in addition to the turbulent viscosity in the source term (Eq. (14)) permits the BVG model to "transition." It is possible to use the data to calibrate a coefficient on the laminar viscosity such that transition occurs at the correct height for the data, but it is unlikely that the results would be general and thus such "tuning" has not been done here.

The strength of the instability will not be independent of the mesh density. Equation (11) indicates that the strength of the instability is proportional to the density gradient crossed with the local pressure gradient. The density gradient is a maximum at the helium/air interface, starting with a discontinuity at the inlet. Finite mesh resolution will limit the maximum resolvable gradient at the inlet. Since the actual gradient will always be much steeper than the mesh-resolved gradient, the resolved gradient will increase with increasing mesh density.

Thus, plumes undergoing a laminar-to-turbulent transition represent a very difficult challenge to turbulence models. As the mesh is refined, the numerical viscosity is reduced and the strength of the instability is increased. Over-prediction of the damping (either by model error or under-

resolved numerics) will result in a plume that spreads too fast. Under-prediction of the damping will result in transient solutions.

5.2 Mesh Dependencies

A possible explanation for the somewhat complex behavior of the simulation results in Figure 8 is that under-resolved numerics can mimic what appears to be a more accurate transition. Even-order truncation error in numerical solutions results in numerical viscosity. Viscosity, whether model or numerically generated, can be expected to have two effects on a transitional plume flow. Increased viscosity will result in broader spreading of the plume momentum and, if it's large enough, can damp out the laminar instability. A more rapid spreading of the plume due to higher viscosity will result in a reduced centerline peak vertical velocity. If the laminar instability is damped, steady solutions will result; if not, transient solutions will result.

Both changes in centerline peak vertical velocity, and steady and unsteady solutions, are presented in Figure 8. The coarsest mesh, 250K, with the highest numerical viscosity has a lower peak vertical velocity than either the data or the higher density mesh results. Increasing the mesh density to 500K (with all else identical) reduces the numerical viscosity. The 500K mesh solution is stable but the peak vertical velocity is above the data. Further increasing the mesh density (and accordingly reducing the numerical viscosity) to 1M and 2M nodes results in unsteady solutions that are density-weighted and time-averaged in Figure 8. As the mesh density increases, from 1M to 2M nodes, the density-weighted, time-averaged centerline velocity just begins to decrease toward the data.

This behavior is not specific to the BVG model. Figure 9 shows results for a similar mesh refinement study for the standard k-ε model for the same problem. The lowest mesh density, 56K, is the only steady k-ε solution shown in Figure 9. All other solutions are transient and have been density-weighted and time-averaged. Increasing the mesh density to 250K, 500K, and 1M results in a higher peak centerline velocity than the 56K mesh result, consistent with expectations of lower numerical viscosity resulting in less plume spreading. As the mesh density is increased from 250K to 500K, the density-weighted, time-averaged results show only a very small decrease in the peak velocity. Increasing the mesh density to 1M nodes resulted in a solution that appeared to be convergent with the 500K mesh results. However, the 2M node mesh, density-weighted, time-averaged solution strongly tends towards the experimental data. Investigating the transient solutions for the 250K, 500K, 1M and 2M node solutions qualitatively shows little difference in the first three transient solutions, while the 2M mesh solution is very dynamic, producing enough puffing to allow the penetration of low-velocity flow into the center of the plume within the window of comparison of the data. This result suggests that improvements in the comparisons with higher mesh density for transient solutions may be the result of mesh-resolved dynamics.

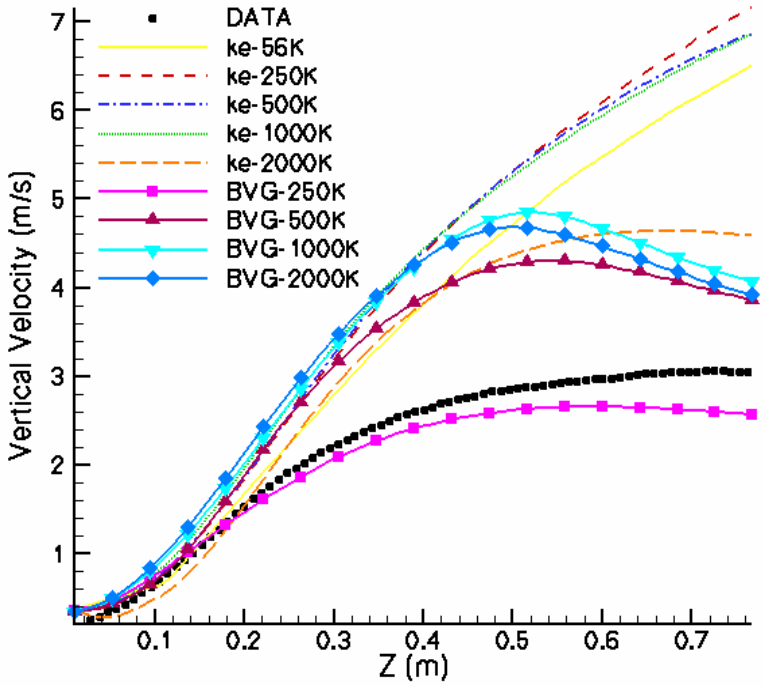

Figure 9. Vertical velocity profiles for k-ε model and BVG model simulations of SNL helium test ensemble. Note that the 250K and 500K mesh BVG solutions are steady, while the other BVG solutions are puffing. For the k-ε results, only the 56K mesh yields a steady solution.

The current time marching scheme in Fuego is only first order in time, consistent with its intended use with Reynolds Averaged Navier-Stokes (RANS) solutions. To address whether the dynamics were due to the first order time scheme, the number of time step sub-iterations (i.e., Picard loops) was varied from 10 to 20 on the 250K mesh. In general, the solutions did not appear to be very sensitive to the number of sub-iterations within a time step.

The BVG results from Figure 8 are overlaid with the k-ε model results in Figure 9. For a given mesh resolution, use of the BVG model results in a better prediction of the data, as expected since more of the physics are captured within the model. While the delayed transition does result in a centerline velocity overshoot for the 500K and higher mesh density results, it is clear from Figure 9 that the BVG results are rapidly tending toward the data as the model transitions. This recovery is attributable to the BVG model in that the 500K mesh result is steady. Only with 2M nodes does the standard k-ε model begin to predict similar quality density-weighted, time-averaged results, and, as stated above, it is very likely that the quality of the prediction is not due to the turbulence model, but the fact that the solution is highly dynamic.

5.3 Best Use of the BVG Model

Numerical and theoretical considerations exist in the use of RANS turbulence models such as the BVG model. From a purely numerical perspective, the best practice is to refine the mesh until a converged solution results. It is clear from the above discussion that this practice is not achievable for practical mesh densities for plumes undergoing laminar-to-turbulent transitions with the models used. In the limit of infinite mesh resolution, it can be expected that both the BVG model and the standard k-ε model will converge to a solution as the laminar instability becomes fully resolved. However, even with 2M nodes it is clear both have significant differences if the solutions are tending to the data (for which there is no guarantee). Thus, from a purely numerical perspective, a pragmatic argument is that best use of the models is to use the highest mesh density that can be achieved.

From a purely theoretical perspective, there is much debate within the community over the meaning of unsteady results for RANS models. It is beyond the scope of this study to put the arguments into perspective; however, two views are relevant. In one perspective, even though the ergodic hypothesis behind RANS filtering of the Navier-Stokes equations has clearly been violated by the transient solutions, it can be argued that the instability causing the transients is laminar, not turbulent, and thus the separation of a mean and fluctuating component representative of turbulence is still valid. A different perspective is that the separation is not strictly valid except under the ergodic hypothesis. Other filtering techniques besides RANS are available and have perhaps a stronger theoretical foundation for transient transitional flows – for example, either a narrower temporal filter (Pruett [20], Pruett et al. [21]) or with a length scale filter (i.e., Large Eddy Simulation, LES, cf. DesJardin, et al. [22]).

The authors are inclined to side with the latter perspective and feel that as the simulation results become increasingly dynamic, the RANS filtering becomes increasingly weaker on theoretical grounds. The authors acknowledge that from a numerical perspective, the best solution is one in which the numerical viscosity is minimized. Balancing both the theoretical and numerical arguments, the authors, as developers of the BVG model, suggest that the best use of the model is to conduct mesh refinement studies until the solution converges or becomes transient, and take the results of the highest mesh density that results in a steady solution. In the case of the higher velocity helium data in Figure 8, that is the 500K mesh. Note that this is not the "best" use of the model as defined by the best comparison with the data, but it is in the authors' opinion the most appropriate. It should also be noted that the mesh that results in the onset of puffing can be a function of the CFD solver used, so stricter guidelines cannot be given.

5.4 Formal Validation of Model

Validation of a model for use in a particular application is an attempt to quantify the uncertainty associated with the use of that model for that application. For helium plumes, of the three model/data comparisons presented, the worst agreement (because of delayed transition) was observed for the ensemble test results (Figure 8). In order to help quantify the comparison between the experimental data and the numerical predictions for the SNL test ensemble, a formal validation metric was developed (Oberkampf and Barone [23]). The validation metric is based on statistical confidence intervals using a student-t distribution for three degrees of freedom, and in

this case is applied to the 500K mesh data. The metric is comprised of the true mean of the experimental data and a confidence interval based on the scatter in the data with 90% confidence that the true mean falls within the interval. The quantity of interest evaluated with the validation metric is the centerline velocity as shown in Figure 10. The effect of the velocity overshoot is readily apparent in the figure, and can be attributed to the delayed prediction of transition, as discussed above. The results indicate that the model predictions are not within the 90% confidence level derived from the data.

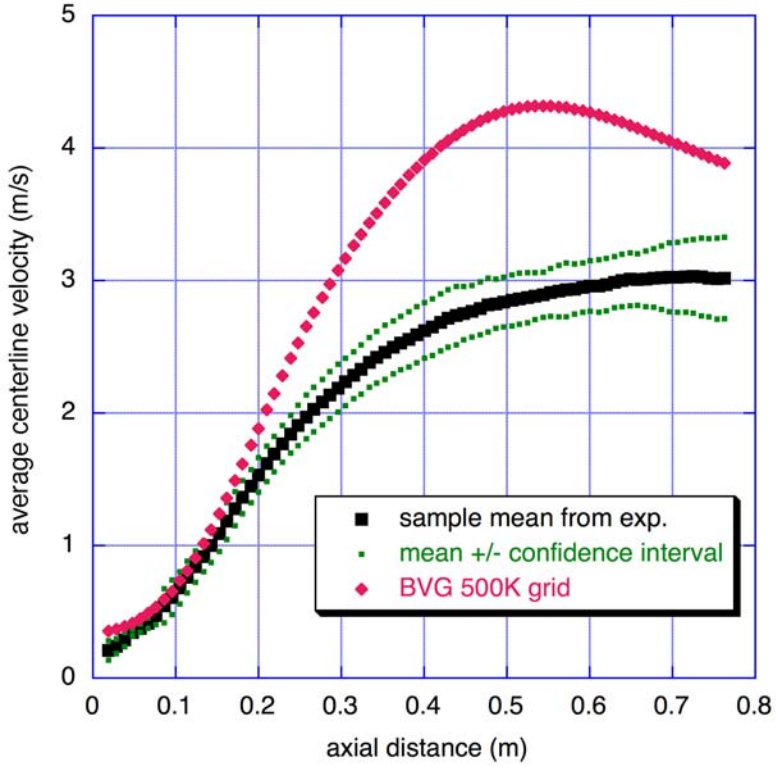

Figure 10. Validation metric comparison for average centerline velocity: Experimental data and BVG model, 500K node mesh, steady solution.

6 CONCLUSIONS

A new model of buoyant turbulence has been developed, implemented, verified, calibrated, and validated. The model postulates that buoyant vorticity generation (BVG) resulting from misalignment of the density and pressure gradients is the key physical mechanism that must be included in a model of buoyant turbulence. The appropriate time scale for buoyant turbulence is taken directly from the baroclinic vorticity generation term in the vorticity equation.

The BVG model has been implemented and verified in a CVFEM formulation for buoyant flows. Calibration of constants in the model was performed using open helium plume data sets obtained at NIST. Validation of the model indicates reasonably good agreement with centerline velocity data for the NIST open helium plume, and for turbulence kinetic energy and vertical velocity profiles for 1-m SNL helium plume experiments. Discrepancies can be accounted for by a laminar-to-turbulent transition in the data that is difficult to model in an eddy viscosity closure context. Grid refinement studies show that the model is more numerically stable and gives better predictions over a much broader range of mesh density than the standard k-ε model for these challenging flows.

7 REFERENCES

1. Cox, G., Turbulent closure and the modeling of fire by using computational fluid dynamics, Phil. Trans. R. Soc. Lond. A, Vol. 356, pp. 2835-2854, 1998.
2. Worthy, J., V. Sanderson, and P. Rubini, Comparison of Modified k-e Turbulence Models for Buoyant Plumes, Numerical Heat Transfer, Part B, vol. 39, pp. 151-165, 2001.
3. Launder, B. E., and D. B. Spalding, The numerical computation of turbulent flows, Computer Methods in Applied Mechanics in Engineering 3, pp. 269-289, 1974.
4. Jones, W. P., and B. E. Launder, The Prediction of Laminarization with a two-equation model of turbulence, *Int. J. Heat Mass Transfer*, Vol. 15, pp. 301-314, 1972.
5. Rodi, W., Turbulence Models and Their Applications in Hydraulics – A State of the Arts Review, University of Karlsruhe, Germany, 1984.
6. Daly, B. J., and F. H. Harlow, Transport Equations in Turbulence, *The Physics of Fluid*s, Vol. 13, no. 11, November 1970.
7. Ince, N. Z. and B. E. Launder, On the computation of buoyancy-driv*en turbulent flows in rectangular enclosures, International Journal of Heat and Fluid Flow*, Vol. 10, no. 2, June 1989.
8. Wang, H. Y., and P. Joulain, Three-Dimensional Modeling for Prediction of Wall Fires with Buoyancy-Induced Flow along a Vertical Rectangular Channel, *Combustion and Flam*e, Vol. 105, pp. 391-406, 1996.
9. Wang, H. Y., P. Joulain, and J. M. Most, Modeling on Burning of large-Scale Vertical Parallel Surfaces with Fire-Induced Flow, *Fire Safety Journal*, Vol. 32, pp. 241-271, 1999.
10. Chomiak, J., and J. R. Nisbet, Modeling Variable Density Effects in Turbulent Flows – Some Basic Considerations, *Combustion and Flame*, Vol. 102, pp. 371-386, 1985.
11. Tieszen, S. R., V. F. Nicolette, L. A. Gritzo, J. K. Holen, D. Murray, and J. L. Moya, *Vortical Structures in Pool Fires: Observation, Speculation, and Simulation*, SAND96-2607, Albuquerque, NM: Sandia National Laboratories, November 1996.
12. Borghi, R., and D. Escudie, Assessment of a Theoretical Model of Turbulent Combustion by Comparison with a Simple Experiment, *Combustion and Flame*, Vol. 56, pp. 149-164, 1984.
13. Domino, S. P., C. D. Moen, S. P. Burns, and G. H. Evans, SIERRA/Fuego: A Multi-Mechanics Fire Environment Simulation Tool, AIAA Paper 2003-0149, 41st AIAA Aerospace Sciences Meeting, Reno, NV, January 2003.
14. Hirsh, C., Numerical Computation of Internal and External Flows, Volume 2. John Wiley & Sons, 1990.
15. Domino, S. P., *SIERRA/Fuego Version 1.00.00 Verification*, internal draft report, Albuquerque, NM: Sandia National Laboratories, October 2003.
16. Fischer, H. B., E. J. List, R.C.Y. Koh, J. Imberger, and N.H. Brooks, Mixing in Inland and Coastal Waters, Academic Press, Chapter 9, pp. 328-332, 1979.

17. Mell, W. E., data of A. Johnson, NIST, as given in the following web page: http://www2.bfrl.nist.gov/userpages/wmell/plumes.html

18. O'Hern, T. J., E. J. Weckman, A. L. Gerhart, S. R. Tieszen, and R. W. Schefer, Experimental Study of a Turbulent Buoyant Helium Plume, in preparation, 2004.

19. Christensen, K. T., S. M. Soloff, and R. J. Adrian, PIV Sleuth – Integrated Particle Image Velocimetry Interrogation/Validation Software, TAM Report No. 943, University of Illinois, 2000.

20. Pruett, C. D., Eulerian Time-Domain Filtering for Spatial Large-Eddy Simulation, AIAA 38(9):1634-1642, 2000.

21. Pruett, C. D., T. B. Gatski, C. E. Grosch, and W. D. Thacker, The temporally filtered Navier-Stokes equations: Properties of the residual stress, *Physics of Fluids*, Vol. 15, no. 8, pp. 2127-2140, 2003.

22. DesJardin, P. E., T. J. O'Hern, and S. R. Tieszen, Large Eddy Simulation and Experimental Measurements of the Near-Field of a Large Turbulent Helium Plume, to appear in *Physics of Fluids*, Vol. 16, no. 5, May 2004.

23. Oberkampf, W. L., and M. F. Barone, "Measures of Agreement Between Computation and Experiment: Validation Metrics," 34th AIAA Fluid Dynamics Conference, Portland, Oregon, June 28- July 1, 2004, paper no. 2004-2626, 2004.

8 DISTRIBUTION

External Distribution

Dr. Geoffrey Cox
FRS, the fire division of BRE
Garston
Watford
WD25 9XX UNITED KINGDOM

Dr. Bjorn Erling Vembe
Computational Industry Tech., A.S.
Haugaastubben 3
Stavanger, NORWAY N-4016

Professor. Bjorn Magnussen
Computational Industry Tech., A.S.
P.O. Box 1275, Pirsenteret
Trondheim, NORWAY N-7462

Professor E. Weckman
Dept. of Mechanical Engineering
University of Waterloo
Waterloo, Ontario
CANADA N2L 3G1

Dr. John de Ris
FM Global Research
1151 Boston-Providence Hwy.
Norwood, MA 02062

Professor Phil Smith
Department of Chemical and Fuels Engineering
University of Utah
Salt Lake City, UT 84112

Professor A. Sarofim
Department of Chemical and Fuels Engineering
University of Utah
Salt Lake City, UT 84112

K.H. Almand, P.E.
Executive Director the Fire Protection Research Foundation
1 Batterymarch Park
Quincy, MA 02169-7471

Internal Distribution

#	MS	Org	Name
1	MS 9052	8367	J. Keller
1	MS 9409	8775	C. Moen
1	MS 9409	8775	G.H. Evans
1	MS 0384	9100	C.W. Peterson
1	MS 0825	9110	W. Hermina
1	MS 0834	9112	T.J. O'Hern
1	MS 0834	9114	M.J. Martinez
1	MS 0834	9114	J. Lash
1	MS 0836	9117	R. Griffith
1	MS 0824	9130	T.Y. Chu
1	MS 1135	9132	L.A. Gritzo
1	MS 1135	9132	S.R. Tieszen
5	MS 1135	9132	V.F. Nicolette
1	MS 1135	9132	A.L. Brown
1	MS 1135	9132	A. Luketa-Hanlin
1	MS 1135	9132	J.C. Hewson
1	MS 0828	9133	M. Pilch
1	MS 0828	9133	A.R. Black
1	MS 0828	9133	W.L. Oberkampf
1	MS 0382	9141	E. Boucheron
1	MS 0382	9141	S.P. Domino
2	MS 9018	8945-1	Central Technical Files
2	MS 0899	4536	Technical Library

This page intentionally left blank


Sandia National Laboratories